ELSEVIER

PII:S0958-9465(98)00012-2

Cement and Concrete Composites **20** (1998) 301–318
0958-9465/98/$ — see front matter

Evaluation of Strains at Peak Stresses in Concrete: A Three-Phase Composite Model Approach

M. A. Tasdemir,[a]* C. Tasdemir,[a] S. Akyüz,[a] A. D. Jefferson,[b] F. D. Lydon,[b] & B. I. G. Barr,[b]

[a]Faculty of Civil Engineering, Istanbul Technical University, Istanbul, Turkey
[b]Division of Civil Engineering, University of Wales Cardiff, UK

(Received 27 August 1997; accepted 23 February 1998)

Abstract

A wide range of concretes was evaluated to explain the reasons for large strain values of high strength concretes (HSCs) at peak stresses under different loading conditions, such as uniaxial compression, uniaxial tension, bending and torsion. To determine the influences of constituents on the stress distributions at the matrix–aggregate interface, around the aggregate and in the matrix close to the aggregate, concrete was considered as a three-phase composite material consisting of a continuous mortar matrix, model aggregate and the interfacial zone between cement and aggregate. The results obtained show that in normal strength concretes (NSCs), i.e. the hard inclusion case, the elastic mismatch of aggregate and matrix is significant and large tangential, radial and shear stresses occur at the interface. However, in both HSCs and lightweight concretes (LCs), the elastic modulus of the aggregate is closer to that of the matrix, and lower tangential, radial and shear stress distributions occur at the aggregate–matrix interface, resulting in these concretes having a much more uniform stress distribution at the interfaces than NSCs. In both HSCs and LCs, tensile stresses occur at the tips of the aggregate (at the poles in the model) perpendicular to the applied stress, and tangential stresses in the matrix close to the interface or at the aggregate surface are larger than those in NSC ones. These imply that the crack will be forced to go through the aggregate and lower strains will develop in ascending branches of these concretes. Based on the model proposed and on additional microstructural studies, it can be concluded that the levels of strains observed at peak stresses under the different loading conditions are as expected. © *1998 Elsevier Science Ltd. All rights reserved.*

Keywords: concrete, peak stresses, peak strains, matrix–aggregate interface, strain capacity, three-phase composite, high strength concretes, lightweight concretes, elastic mismatch, tangential stresses, interfacial microstructure.

INTRODUCTION

In recent years, three developments have permitted modern concrete to approach its potential as a structural material, namely the better understanding of preventative measures against damaging mechanisms (such as freeze/thaw cycling, embedded steel corrosion and AAR), the use of superplasticizers (for rheological control and to lower the water–cement ratio of the mixture) and the inclusion of silica fume (to enhance overall durability and strength).[1]

The use of concrete for special structures such as long span bridges, dams, nuclear reactors, offshore structures and storage tanks has led to growing interest in the cracking behaviour of concrete. In some loading condi-

*To whom correspondence should be addressed.

tions, strains at peak stresses are required for calculating the response of a structure, for crack control and determining the risk of cracking.[2] Such strains in direct tension, bending, uniaxial compression and torsion are evaluated as shown below considering both material behaviour and its modelling.

Material behaviour

An accurate value of the strain at maximum stress is important for the stress–strain curve of concrete under uniaxial compression. De Nicola *et al.*[3] proposed a nonlinear relationship between compressive strength and the strain at maximum stress.

Since concrete is weak in tension, its tensile strength is frequently neglected in the conventional design of reinforced concrete structures. During the last two decades, research on concrete primarily concentrated on increasing its compressive strength; however, for a better understanding of material behaviour more information is needed regarding many aspects of mechanical properties, such as fracture behaviour and tensile properties.[2]

In bending, good correlations have been obtained between flexural tensile strain capacity defined in different ways and flexural strength for various ages.[4,5] The flexural tensile strain capacity of concretes with compressive strength reaching up to 80 N/mm^2 was investigated by Giovambattista *et al.*[6] under rapid and slow loading rates. They showed that the tensile strain capacity in bending increases with concrete strength. Brooks *et al.*[7] indicated that the thermal strain capacity of concretes of similar strength and workability is related to the type of coarse aggregate used, and there was good correlation between strain capacity and 'strength/modulus of elasticity' for these results. Based on recent advances, Tasdemir *et al.*[2] gave a comprehensive review of the behaviour of concrete in tension and the major role of tensile properties in the fracture of concrete. For a wide range of unnotched concrete specimens, it was shown by them that the short term strain capacity under direct tension can be predicted from the 'tensile strength/modulus of elasticity' ratio which was in good agreement with published results and was virtually independent of experimental techniques, type, size and grading of aggregate, gauge length, age and loading rate. Hence, sufficient data on a very wide range of concretes are now available for analysis of the strains at peak stresses in concretes for different loading configurations, such as uniaxial tension, bending, torsion and uniaxial compression.

Material modelling

Concrete is an extremely complex system of solid phases, pores and water, with a high degree of heterogeneity. This heterogeneity can be considered on several levels. For material modelling purposes, Wittmann[8] introduced the idea of three levels: micro-, meso- and macro-levels. To establish a realistic failure model at the macro-level, an insight into the fracture mechanisms at the meso-level is required, where heterogeneity results in a non-uniform internal strain distribution within the concrete composites. Recent research[1,9,10] has shown that there are two principal aspects of interfaces in concrete: (i) the microstructural features of the interfacial region and their effects on concrete properties; and (ii) models of the effects of interfaces on the properties of concrete through the application of continuum mechanics and fracture mechanics. Since the interface between the aggregates and cement paste is the weakest link, the mechanical behaviour of concrete is significantly affected by the properties of the interfacial zone, being especially sensitive to the properties of this zone.[1,9–11] The interface failure may be considered at the meso-level. The development of bond cracks at the aggregate–matrix interfaces plays an important role in the inelastic behaviour of concrete. A considerable portion of the total strain is concentrated at the interfaces and the final failure occurs in mortar, thus bridging bond cracks.[12–14]

The main objective of this work is to explain the reasons for the levels of strain values at peak stresses. To provide quantitative results, more data on a wide range of concretes were evaluated in the light of the material model proposed, and some microstructural studies were also used for a better understanding of the material behaviour under different loading conditions, such as uniaxial tension, bending, torsion and uniaxial compression. To determine the influence of this interfacial zone on the stress distributions at the matrix–aggregate interface, concrete was considered as a three-phase composite material consisting of a

continuous mortar matrix phase, a model aggregate and an interfacial zone between the cement paste and the aggregate. To support the explanations for high strain values at the peak stresses of HSCs, microstructural studies were also used, based on Scanning Electron Microscope (SEM) and Energy Dispersive X-Ray Analyzer (EDX) observations.

EVALUATIONS OF STRAINS AT PEAK STRESSES

Concrete shows an inelastic behaviour under short-term compressive loading. Considerable effort has been spent on this behaviour under static uniaxial loading for about 70 years. The contact zone (the interface between the matrix and aggregate phases) was found to play an important role in the shape of the stress–strain curve under uniaxial compression being explained by progressive microcracking in the concrete. Microcracks start on the interfaces and as the load is increased the bond cracks penetrate into the mortar matrix. Then, the interconnected network of bond and matrix cracks results in material discontinuity and any further load increase produces failure.[15,16] Based on the results of three different research groups, typical stress–strain curves for a wide range of concretes are represented in Fig. 1,[16–18] where the linearity of the ascending part of the curves increases with increasing compressive strength. The curves of concretes having high compressive strength are almost linear up to peak stress. It is seen that the axial strain capacity increases significantly in HSCs, that there is a sudden drop of stress and that they fail in a more brittle manner. Fig. 1 also shows that the relative increase in the modulus of elasticity is considerably lower than the relative increase in compressive strength. For high strength concretes, the relative absorbed energy up to peak stress is lower than that of lower strength concretes; this is explained below.

Energy absorption capacity in compression was determined by calculating the area under the stress–strain curve up to peak stress. In the ascending portion of this curve, both stress and strain axes were normalized, dividing by the compressive strength (f_c') and ultimate strain (ε_u) as shown in the inset of Fig. 2. Thus, based on the normalized curve, the relative absorbed energy (U_r) can be calculated by

$$U_r = \frac{\int_0^{\varepsilon_u} \sigma(\varepsilon)\mathrm{d}\varepsilon}{f_c'\varepsilon_u} \tag{1}$$

As seen in the inset of Fig. 2, the line OP is the diagonal of the rectangular OAPB. If the material is perfectly linear-elastic, the curve will be OP; if the curve follows the OBP path, then the material behaviour will be perfectly plastic. Thus, the relative absorbed energy, U_r, lies between 0.5 and 1, i.e. $0.5 < U_r < 1$. If the curve follows ONP instead of OMP, that means that the behaviour of the concrete is more brittle. Fig. 2 shows that as the compressive strength increases, the relative absorbed energy up to

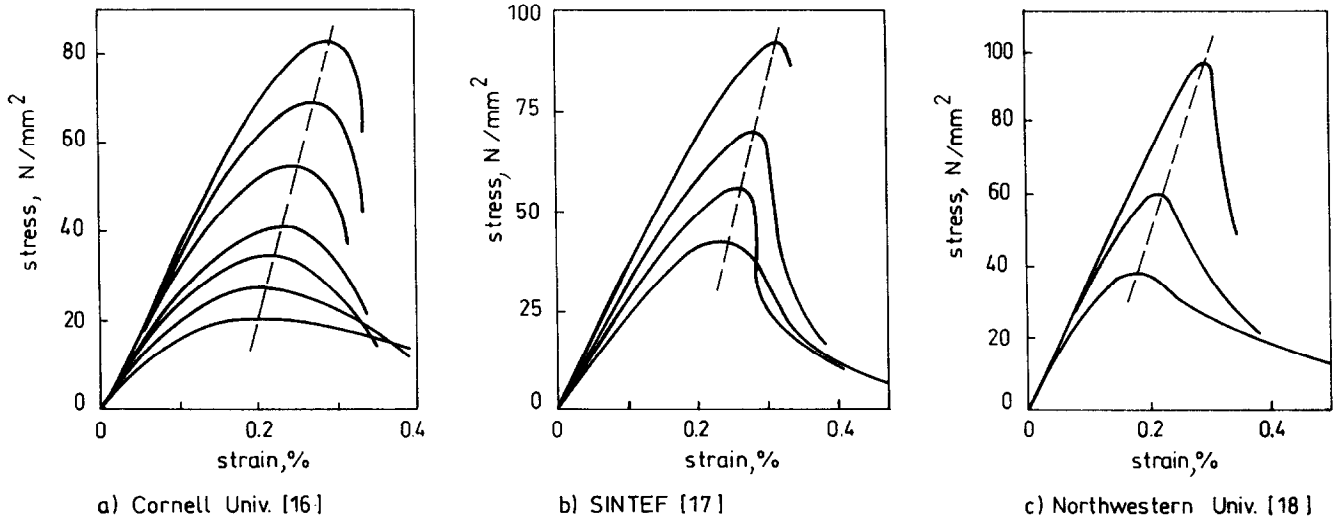

Fig. 1. Stress–strain curves in uniaxial compression based on three different research groups.[16–18]

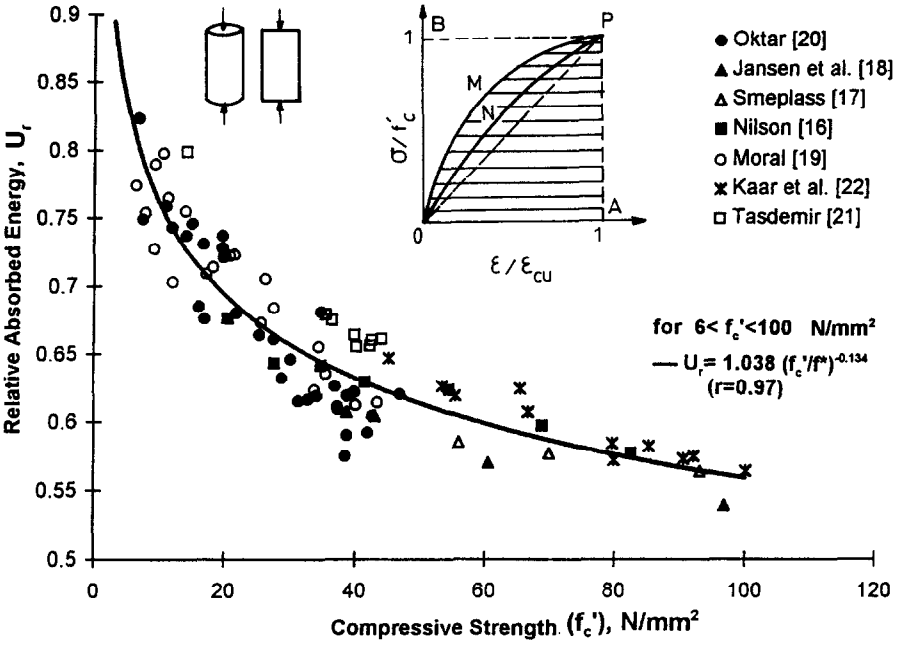

Fig. 2. Relative fracture energy versus compressive strength.

peak stress decreases significantly. Hence, the relative energy, U_r, may be represented by

$$U_r = 1.038(f_c'/f^*)^{-0.134} \quad (2)$$

where $f^* = 1$ N/mm^2. In the relation shown by eqn (2), the correlation is high (0.97) and the equation is valid for a range of compressive strengths from 6 to 100 N/mm^2. For the analysis of relative absorbed energy, 85 different concrete test results from Refs [16–22] under uniaxial compressive loading were used. Details of the data analyzed are given in Table 1. All the

Table 1. Some details of uniaxial compression tests

Source reference	*Specimen size (mm)*	*Age (days)*	*Type of coarse aggregate*	*Variables studied*
Smeplass (1992)[17]	ϕ150 × 300 cylinders	28	Crushed gravel	W/C ratio, cement content
Jansen *et al.* (1995)[18]	ϕ102 × 203 cylinders	56	Gravel	W/Binder ratio
Moral (1979)[19]	ϕ152 × 305 cylinders	105	Gravel	Aggregate grading
Oktar (1977)[20]	ϕ152 × 305 cylinders	180	Gravel	Structure of binding, W/C ratio
Tasdemir (1982)[21]	ϕ152 × 305 cylinders	28	Pumice, limestone	W/C ratio, aggregate fraction, density of concrete
Kaar *et al.* (1977)[22]	ϕ152 × 305 cylinders	Not given	Gravel, limestone, lightweight agg.	W/C ratio, strength
Yildirim (1989)[23]	ϕ152 × 305 cylinders	28	Limestone, pumice	Aggregate fraction
Bischoff and Perry (1995)[a24]	ϕ102 × 254 cylinders	40	Gravel	Loading rate and strength
Carrasquillo *et al.* (1981)[25]	ϕ152 × 305, ϕ102 × 203 cylinders	56	Gravel, limestone	W/C ratio, strength
Dilger *et al.* (1984)[b26]	152 × 152 × 610 prisms	40	Not given	Stain rate
Ahmad and Shah (1985)[b27]	ϕ76 × 305, ϕ152 × 305 cylinders	28, 55	Crushed stone, expanded clay, expanded shale	W/C ratio, strain rate, type of aggregate
Ahmad and Shah (1982)[b28]	ϕ76 × 305 cylinders	28–200	Crushed stone, expanded clay and shale	W/C ratio, strain rate, type of aggregate
Smeplass (1992)[29]	ϕ150 × 300 cylinders	7, 28	Lightweight aggregate (Liapor)	W/C ratio, cement content

[a]Static test results were used.
[b]Unreinforced specimens were used only.

results were based on closed-loop displacement controlled test conditions on the cylinders or on the prisms.

Strain at compressive strength (ε_{cu})

In some design codes, the strain at peak stress in uniaxial compression is assumed to be about 0.002.[3] However, the strain at compressive strength depends on the mix composition, curing conditions, shape and size of specimen, loading rate, age of loading, and test techniques used. To provide quantitative results, more published data on a wide range of concretes were evaluated. For the analysis, a total of 228 different test results were used from Refs [17,19–29] under uniaxial compressive loading conditions. Some details are given in Table 1.

As seen in Fig. 3, in spite of considerable scatter, there is a significant trend showing that as the compressive strength of concrete increases the strain at peak stress increases. A polynomial function ($\varepsilon_{cu} = -0.067(f_c'/f^*)^2 + 29.9(f_c'/f^*) + 1053 \times 10^{-6}$) was fitted to the experimental data and a reasonably good correlation coefficient of 0.75 was found for a range of compressive strength from 6 to 105 N/mm^2, where ε_{cu} is the strain at compressive strength, $f^* = 1$ N/mm^2 and f_c' is the cylinder or prism compressive strength in N/mm^2.

Tensile strain capacity (ε_{tu})

The tensile strain capacity of concrete, defined as a measure of the ability of the material to withstand deformation without cracking, is essential for reducing the risk of cracking under service load conditions. In order to evaluate some tensile strain capacity values for a wide-range of concretes, unnotched prism specimens with or without reduced cross-sections were used. Some details of experimental results based on 90 sets of data from Refs [17,29–33] are given in Table 2. Figure 4 shows that the tensile strain capacity (ε_{tu}) increases with increasing compressive strength. A polynomial function ($\varepsilon_{fu} = -0.009(f_c'/f^*)^2 + 2.633(f_c'/f^*) + 45.7 \times 10^{-6}$) was fitted to the published data for a range of compressive strengths from 10 to 105 N/mm^2. In this relation the correlation coefficient is 0.90.

Flexural strain capacity (ε_{fu})

A limited amount of experimental data on flexural tensile strain capacity is available.[4–6] For

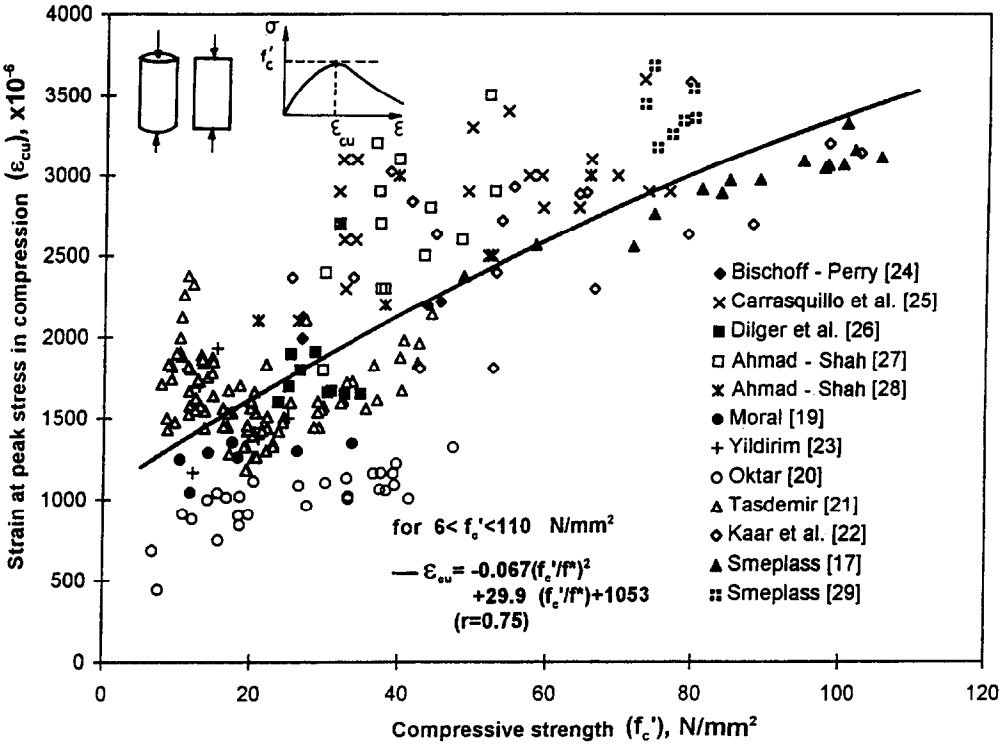

Fig. 3. Strain at peak stress in compression versus compressive strength.

Table 2. Some details of uniaxial tensile tests

Source reference	*Specimen size (mm)*	*Age (days)*	*Gauge length (mm)*	*Type of coarse aggregates*	*Variables studied*
Smeplass (1992)[17]	100 × 100 × 600 prisms	28	100	Crushed gravel	W/C ratio, cement content
Smeplass (1992)[29]	100 × 100 × 600 prisms	28	100	Lightweight aggregates (Liapor)	W/C ratio, cement content
Balendran (1980)[30]	102 × 102 × 508 prisms (eff.cs[a] 102 × 76)	7 and 28	203	Crushed limestone; sintered pfa sintered (pfa+clinker)	A/C ratio, W/C ratio
Phillips and Zhang (1993)[31]	100 × 150 × 70 prisms (eff.cs 100 × 100)	28	100, 150, 300	Gravel	A/C ratio, W/C ratio
Guo and Zhang (1987)[32]	70 × 70 × 148 prisms (eff.cs 40 × 40)	36–40	40	Gravel	Type of cement
Xie and Liu (1989)[33]	550 × 550 × 3600 prisms (eff.cs 450 × 450)	28	400	Gravel	A/C ratio, W/C ratio
	100 × 100 × 550 prisms (eff. cs 100 × 100)	28	Not given	Gravel	A/C ratio, W/C ratio

[a]Effective cross section.

this analysis, a total of 32 experimental results were used which were measured at about 95% of the ultimate load[4,6] or at cracking.[5] Details of the data evaluated are given in Table 3. As seen in Fig. 5, the flexural tensile strain capacity also increases with increasing compressive strength of the concrete. A polynomial function ($\varepsilon_{fu} = -0.0007(f_c'/f^*)^2 + 1.825(f_c'/f^*) + 67.7 \times$

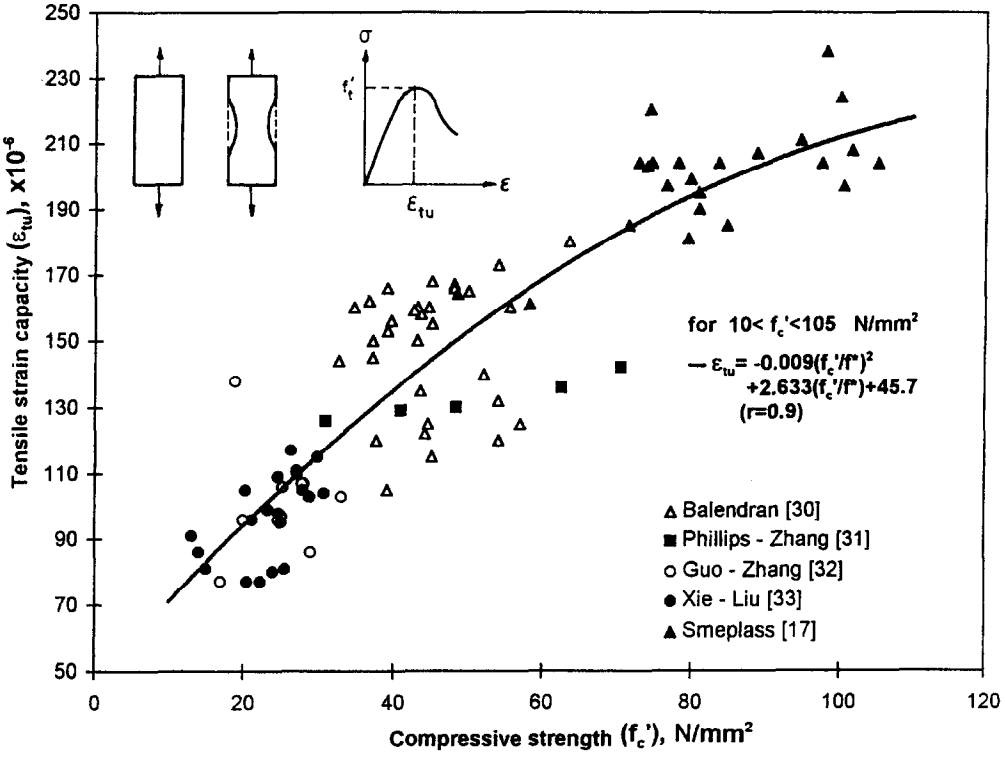

Fig. 4. Tensile strain capacity versus compressive strength.

Table 3. Some details of bending tests

Source reference	*Specimen size (mm)*	*Age (days)*	*Gauge length (mm)*	*Type of coarse aggregate*	*Variables studied*
Welch (1966)[4]	102 × 102 × 508 beams	28	50	Gravel, granite	W/C ratio
Oladapo (1964)[5]	100 × 100 × 600 beams	14	25.4	Gravel	W/C ratio, cement content
Giovambattista *et al.* (1992)[6]	150 × 150 × 900 beams	1, 28	250	Granite, basalt	W/C ratio

10^{-6}) was fitted to the data for a range of compressive strengths from 5 to 85 N/mm^2. In this relation, the coefficient of correlation is 0.84.

Torsional strain capacity (ε_{su})

Little information on the torsional strain capacity of concrete is available in the literature. The results evaluated here were based on the strain capacities obtained via a torsion test rig developed at the University of Wales Cardiff, as illustrated in the inset of Fig. 6. Intensive work was carried out on stiffness and torsional damage tests under different ages and curing conditions. Also, a comparative study was done in conjuction with the Building Research Establishment (BRE) for a wide range of concretes.[34] However, in Fig. 6 only the torsional strain capacities and corresponding compressive strength values were evaluated for the purpose of this work. In spite of limited experiments, as seen in Fig. 6, there is a good relationship between the cylinder compressive strength (f_c') and the torsional strain capacity given by ($\varepsilon_{su} = -0.0005(f_c'/f^*)^2 + 1.05(f_c'/f^*) + 245.6 \times 10^{-6}$ for $37 < f_c' < 110$ N/mm^2), the correlation coefficient being 0.97. Brokenshire[34] has shown that there is very good relation between torsional strength and compressive strength of concrete, as indicated in the inset of Fig. 7. By using his test results, it can be concluded that as the shear strength increases, the torsional strain capacity increases significantly, as seen in Fig. 7. These results also confirm that the peak strain in torsion increases with increasing strength. Finally, Figs 3–7 show that the higher the compressive strength the higher the strains at peak stresses in compression, tension, bending and torsion for a wide-range of concrete strengths. These observations further motivated investigations into the role of the interface, elastic mismatch of aggregate and matrix in concretes. Based on the stress distributions around the aggregate using a three-phase composite

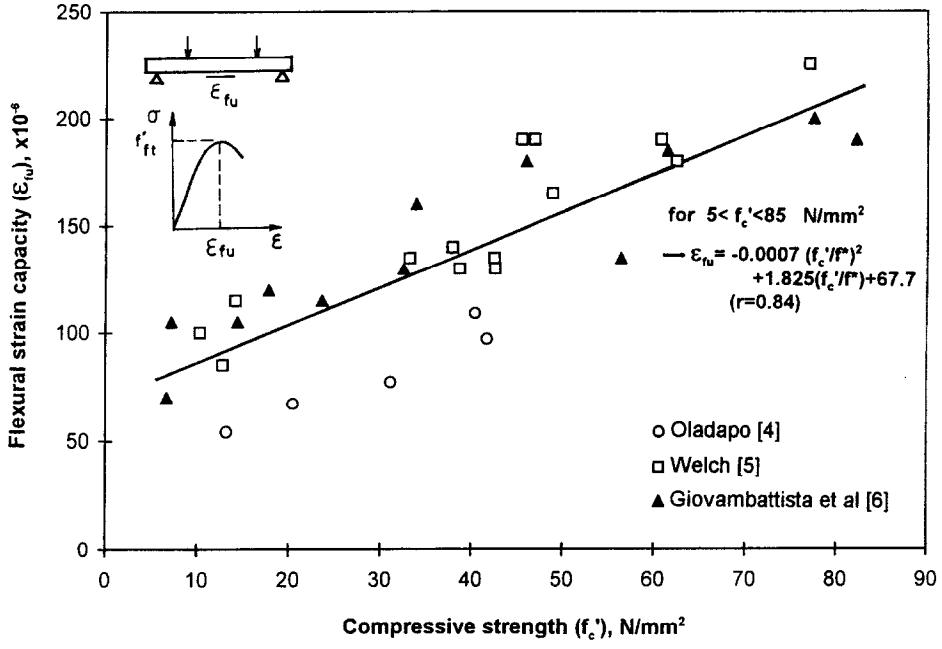

Fig. 5. Flexural strain capacity versus compressive strength.

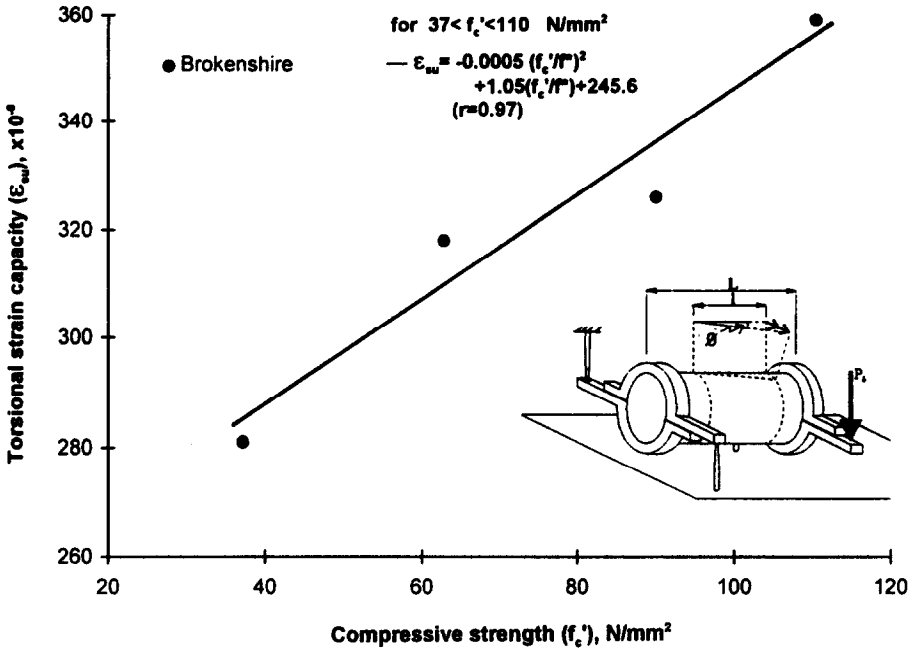

Fig. 6. Torsional strain capacity versus compressive strength.

material model proposed here, the dependency of strains at peak stresses on the compressive strength of the concrete will be explained below.

THREE-PHASE COMPOSITE MODEL PROPOSED

Model proposed

Conventionally, concrete is considered as a two-phase composite material which consists of coarse aggregate and the surrounding continuous mortar matrix. Such a two-phase model with centred model aggregate can be presented in the disc specimen shown in Fig. 8(a). In normal strength concretes (NSCs) the elastic modulus and the strength of the matrix are less than that of most normal weight aggregates. However, the particle strengths, moduli of elasticity and densities of lightweight aggregates are naturally less than those of normal weight aggregates. As pointed out by Bremner,[35] in NSCs, the elastic mismatch of aggregate and matrix causes stress concentrations when the

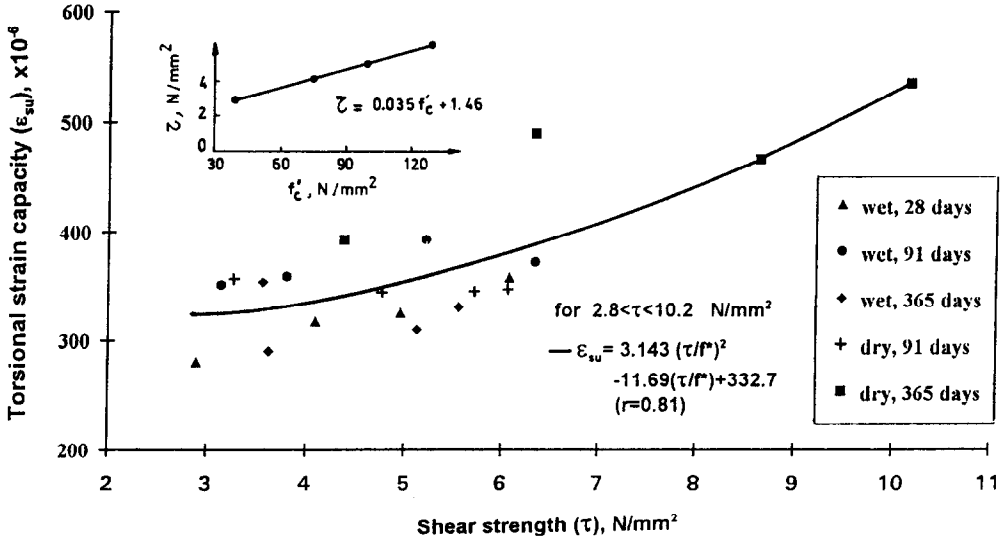

Fig. 7. Torsional strain capacity versus shear strength.

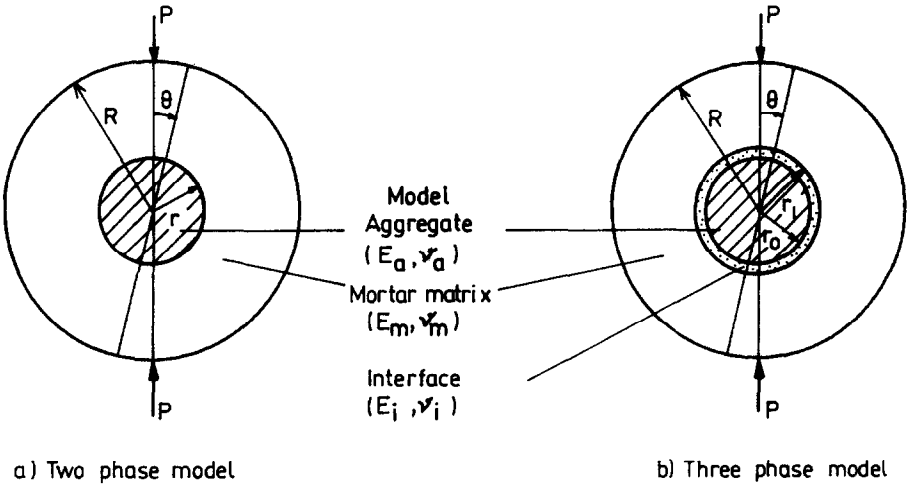

Fig. 8. Two-phase and three-phase composite material models in disc specimens.

composite is subjected to external loads. Since the interface between the aggregates and the cement paste is the weakest link, the mechanical behaviour of NSCs is largely affected by the properties of the interfacial zone. Hence, it is necessary to include the interfacial zone as a third phase in NSCs for a better understanding of material behaviour and also for material modelling purposes.

As shown in Fig. 8(b), a three-phase composite material model which consists of a cylindrical model aggregate and concentric cylindrical shells is proposed. The model aggregate is located at the centre of the disc with the surrounding thin wall matrix–aggregate interfacial zone, and the thick outer shell as the bulk matrix phase. The stress distributions in these zones were obtained as functions of E_m/E_i and E_a/E_i ratios, where E_m, E_i and E_a are the moduli of elasticity of the matrix, interfacial zone and aggregate, respectively. The calculations are based on the theory of elasticity and the assumption of isotropy and small deformation. The three-phase composite model is, mainly, based on the work done by Tasdemir,[36] derived from the solutions of Akyüz.[37,38] The stress distributions were found in plane stress conditions for $E_m < E_a$ and $E_m > E_a$. As shown in Fig. 8(b), $r_1 - r_0$ is the thickness of the matrix–aggregate interface, r_0 and R are the radii of the model aggregate and the disc, respectively. Consider a ring zone with inner and outer radii r and R, respectively, as indicated in Fig. 8(a). Based on the diametral compressive loading, the stresses and strains belonging to this zone can be represented as follows.[39,40]

(i) Radial (σ_{rr}), tangential ($\sigma_{\theta\theta}$) and shear stresses ($\sigma_{r\theta}$):

$$\sigma_{rr}(\theta,r)=\frac{b_0}{r^2}+2c_0-\sum_{n=1}^{\infty}\{a_{2n}2n(2n-1)r^{2n-2}+b_{2n}(2n+1)(2n-2)r^{2n}+c_{2n}2n(2n+1)r^{-(2n+2)}+d_{2n}(2n-1)(2n+2)r^{-2n}\}\cos 2n\theta \quad (3)$$

$$\sigma_{\theta\theta}(\theta,r)=-\frac{b_0}{r^2}+2c_0+\sum_{n=1}^{\infty}\{a_{2n}2n(2n-1)r^{2n-2}+b_{2n}(2n+1)(2n+2)r^{2n}+c_{2n}2n(2n+1)r^{-(2n+2)}+d_{2n}(2n-2)(2n-1)r^{-2n}\}\cos 2n\theta \quad (4)$$

$$\sigma_{r\theta}(\theta,r)=\sum_{n=1}^{\infty}\{a_{2n}2n(2n-1)r^{2n-2}+b_{2n}(2n+1)r^{2n}-c_{2n}2n(2n+1)r^{-(2n+2)}-d_{2n}2n(2n-1)r^{-2n}\}\sin 2n\theta \quad (5)$$

(ii) Radial (U_r) and tangential (U_θ) displacements:

$$U_r(\theta,r)=\frac{1}{E}\left\{-\frac{b_0}{r}(1+\nu)+2c_0(1-\nu)r+\sum_{n=1}^{\infty}[a_{2n}2n(1+\nu)r^{2n-1}+b_{2n}[(2n-2)+\nu(2n+2)]r^{2n+1}-c_{2n}2n(1+\nu)r^{-(2n+1)}\right.$$

$$-d_{2n}[(2n+2)+\nu(2n-2)]r^{-(2n-1)}]$$

$$\times \cos 2n\theta\Big\} \quad (6)$$

$$U_\theta(\theta,r)=\frac{1}{E}\Big\{\sum_{n=1}^{\infty}[a_{2n}2n(1+\nu)r^{2n-1}$$

$$+b_{2n}[2n(1+\nu)+4]r^{2n+1}$$

$$+c_{2n}2n(1+\nu)r^{-(2n+1)}$$

$$+d_{2n}[2n(1+\nu)-4]r^{-(2n-1)}]\sin 2n\theta\Big\} \quad (7)$$

For the interfacial transition zone, equations of stresses and displacements are similar to those given in eqns (3)–(7), however, all the constants have the single mark (′) such as a_{2n}', b_{2n}', c_{2n}' etc. For the shaded zone which is the model aggregate at the centre of radius r, the stresses and displacements can be written as follows:

(i) Radial (σ_{rr}), tangential (σ_{00}) and shear ($\sigma_{r\theta}$) stresses:

$$\sigma_{rr}(\theta,r)=2c_0''-\sum_{n=1}^{\infty}\{a_{2n}''2n(2n-1)r^{2n-2}$$

$$+b_{2n}''(2n+1)(2n-2)r^{2n}\}\cos 2n\theta \quad (8)$$

$$\sigma_{00}(\theta,r)=2c_0''+\sum_{n=1}^{\infty}\{a_{2n}''2n(2n-1)r^{2n-2}$$

$$+b_{2n}''(2n+1)(2n+2)r^{2n}\}\cos 2n\theta \quad (9)$$

$$\sigma_{r\theta}(\theta,r)=\sum_{n=1}^{\infty}\{a_{2n}''2n(2n-1)r^{2n-2}$$

$$+b_{2n}''2n(2n+1)r^{2n}\}\sin 2n\theta \quad (10)$$

(ii) Radial (U_r) and tangential (U_θ) displacements:

$$U_r(\theta,r)=\frac{1}{E}\Big\{2c_0''(1-\nu)r+\sum_{n=1}^{\infty}[a_{2n}''2n(1+\nu)r^{2n-1}$$

$$+b_{2n}''[(2n-2)+\nu(2n+2)]r^{2n+1}]\cos 2n\theta\Big\} \quad (11)$$

$$U_\theta(\theta,r)=\frac{1}{E}\Big\{\sum_{n=1}^{\infty}[a_{2n}''2n(1+\nu)r^{2n-1}$$

$$+b_{2n}''[2n(1+\nu)+4]r^{2n+1}]\sin 2n\theta\Big\} \quad (12)$$

For the model in Fig. 8(b), the following assumption at the boundaries can be written as:

at $r=R$

$$\sigma_{rr}=-\frac{P}{\pi R}\sum_{n=1}^{\infty}\cos 2n\theta;\ \sigma_{r\theta}=0 \quad (13)$$

at $r=r_1$

σ_{rr} (matrix) = σ_{rr} (interface)
$\sigma_{r\theta}$ (matrix) = $\sigma_{r\theta}$ (interface)
U_r(matrix) = U_r (interface)
U_θ (matrix) = U_θ (interface)

at $r=r_0$

σ_{rr} (interface) = σ_{rr} (aggregate)
$\sigma_{r\theta}$ (interface) = $\sigma_{r\theta}$ (aggregate)
U_r (interface) = U_r (aggregate)
U_θ (interface) = U_θ (aggregate)

From the sets of equations given, for $n=0$, b_0, c_0, b_0', c_0' and c_0''; for $n=1$, a_2, b_2, c_2, d_2, a_2', b_2', c_2', d_2', a_2'' and b_2''; for $n=2$, a_4, b_4, c_4, d_4, a_4', b_4', c_4', d_4', a_4'' and b_4'' were found. Hence, while n takes 3, 4, 5, ..., the other coefficients can also be obtained. The angle was given values from 0° to 90° to calculate the stress distributions around the model aggregate.

Model experiments

The objective of these experiments was to investigate the influence of the partial replacement of cement by silica fume on the interface between a model aggregate of diameter 30 mm and matrix in a cast specimen as shown in Fig. 9. Mix proportions of mortars with and without silica fume were 1:2:0.10:0.0084:0.36 and 1:2:0.0:0.013:0.36 (cement:sand:silica fume: superplasticizer:water) by weight, respectively. The maximum particle size of sand was 2 mm. The silica fume with 95% SiO_2 was used in a slurry form. The water–binder ratio was kept at 0.36 in both mixes. Ordinary Portland Cement PC 32.5 and a sodium naphthalene sulphonate type superplasticizer were used for the mixes. Specimens were cast in a specially designed

steel mould and were cured in water, saturated with lime, for 26 days. At least five specimens of each mix were tested under diametral compression at 28 days. During these diametral compression disc tests, the strains were measured using strain gauges at the critical points having high values of tangential and radial stresses. Mechanical properties of the model aggregates are given in Table 4. For all constituents, a value of 0.2 was used for the Poisson ratio.

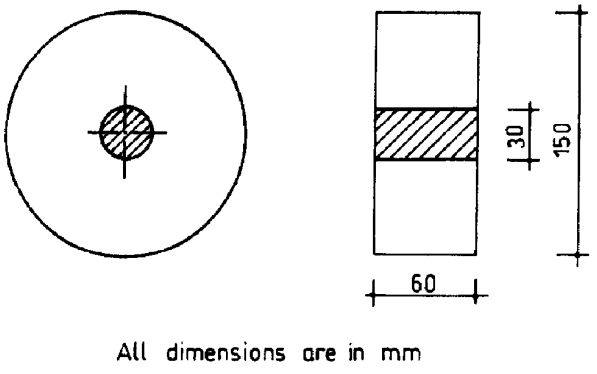

Fig. 9. Dimensions of disc specimens.

Stress distributions around aggregate

The angle θ, with respect to the loading direction in the disc, takes the values from 0° to 90° to calculate the stress distributions around the aggregate using coefficients obtained for different values n mentioned above. The stress distributions were found on the basis of a unit applied stress to the disc specimen.

For the disc specimen containing the hard inclusion in the soft matrix, the stress distributions shown in Fig. 10 were obtained using $E_m/E_i = 6$, $E_a/E_i = 14$, $\nu = 0.20$, $R = 75$ mm, $r_0 = 15$ mm, $r_1 = 15.06$ mm and $P = 1$ kN/mm.

Table 4. Mechanical properties of constituents phases

Mechanical property	*Mortar matrix*		*Model aggregate*
	Without silica fume	*With silica fume*	
Modulus of elasticity (kN/mm^2)	32.4	37.8	70.0
Compressive strength (N/mm^2)	59.8	64.3	92.0

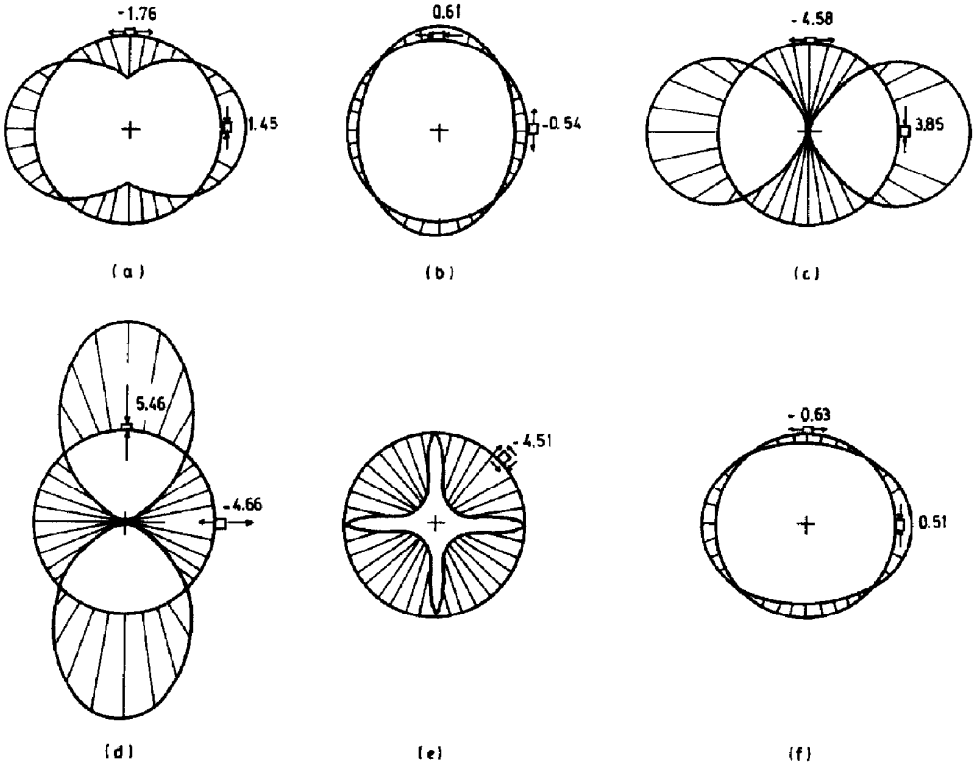

Fig. 10. Stress distributions (s.ds) in soft matrix and around a hard inclusion: (a) tangential s.ds in the matrix close to the interface; (b) tangential s.ds at the interface; (c) tangential s.ds at the aggregate surface; (d) radial s.ds in the matrix close to the interface, at the interface and on the aggregate surface; (e) shear s.ds in the zones shown in (d); (f) tangential s.ds at the interface for HSCs.

For the soft inclusion case these values were $E_m/E_i = 6$, $E_a/E_i = 5$, $v = 0.2$, $R = 75$ mm, $r_0 = 15$ mm, $r_1 = 15.06$ mm and $P = 1$ kN/mm. As seen in Fig. 10(a) and (c) and Fig. 11(a) and (c), for both hard and soft inclusion cases, tangential stresses at the matrix side of the interface or at the surface of the model aggregate, at the poles ($\theta = 0°$) are tensile, whereas at the equator ($\theta = 90°$) these stresses are compressive. In the soft inclusion case, it is seen that tangential stresses in the matrix close to the interface or at the aggregate surface are higher than those of the hard inclusion cases.

In specimens with a hard inclusion as in Fig. 10(b), (d) and (e), it is observed that high values of tangential, radial and shear stress concentration are developed at the interface due to the large differences in the elastic moduli of the aggregate and mortar matrix. As shown in Fig. 11(b), (d) and (e), however, in specimens with a soft inclusion, since the elastic modulus of the aggregate is close to that of the mortar matrix, lower stress concentrations occur at the aggregate–matrix interface. As seen in Fig. 11(b) in the soft inclusion case tangential stresses were tensile at the pole and compressive at the equator, whereas, as seen in Fig. 10(b), opposite results were obtained in the hard inclusion case.

The results obtained show that in NSCs (the hard inclusion case) the elastic mismatch of the aggregate and the matrix is significant and large tangential, radial and shear stresses occur at the interface. However, in lightweight concretes (LCs), the elastic modulus of the aggregate is close to that of the matrix, hence lower tangential, radial and shear stress concentrations develop and low stress distributions occur at the aggregate–matrix interface. As pointed out by Bremner and Holm,[41] this results in these concretes having a much more uniform stress distributions at the interfaces as compared to NSCs. In both HSCs and LCs, tensile stresses occur at the tip of the aggregate (at the pole in the model) perpendicular to the applied load, and tangential stresses in the matrix close to the interface are larger than those of NSC ones. These imply that a crack occurring at the interface may penetrate into the matrix, and may be forced to pass through the aggregate; as a result lower strains will develop at the interface, as compared to NSCs, thus less stress-induced microcracking will be obtained in ascending branches of these concretes. In the calculations of stress distributions, the elastic modulus of the interface between the matrix and model aggregate was assumed to be 5 kN/mm^2 for

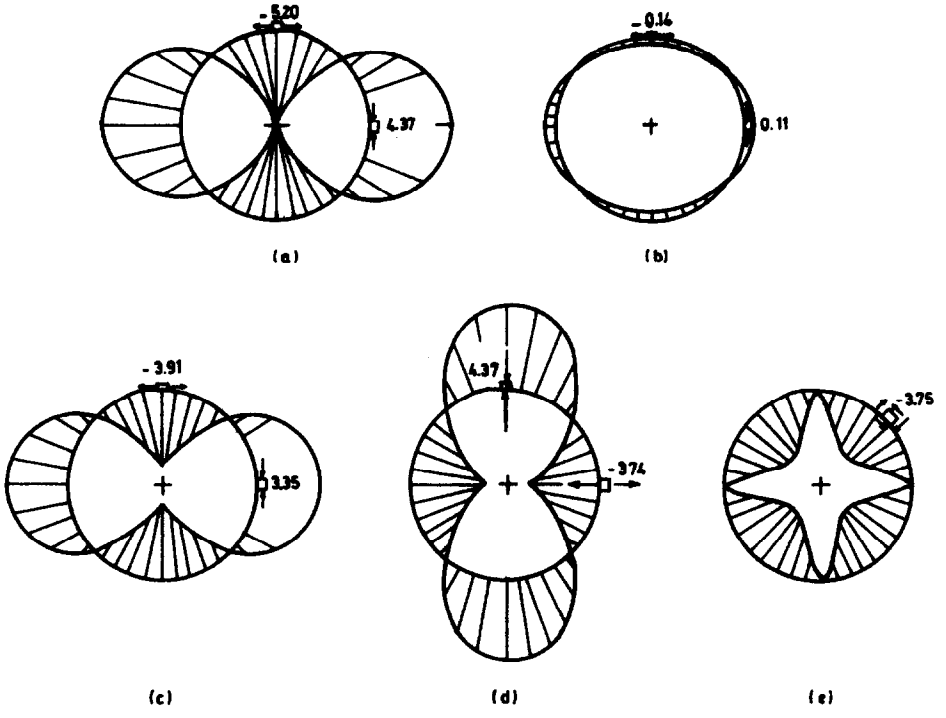

Fig. 11. Stress distributions (s.ds) in a hard matrix and around a soft inclusion: (a) tangential s.ds in the matrix close to the interface; (b) tangential s.ds at the interface; (c) tangential s.ds at the aggregate surface; (d) radial s.ds in the matrix close to the interface, at the interface and on the aggregate surface; (e) shear s.ds in the zones shown in (d).

specimens without silica fume and 20 kN/mm^2 for specimens with silica fume. Based on the strain measurements and calculations at the interface, it can be concluded that the thickness of the interface decreases in specimens with silica fume. In Fig. 10(f), stress distributions were calculated in the case of $E_m/E_i = 2$, $E_a/E_i = 3.5$, $\nu = 0.2$, $R = 75$ mm, $r_0 = 15$ mm, $r_1 = 15.03$ mm and $P = 1$ kN/mm, which provided closer stiffness for both the matrix and model aggregate and the lower interface thickness. From a stress concentration point of view, this is a typical indication for high strength concrete. Low stress concentrations develop at the interface. Use of a superplasticizer and silica fume will enhance the interface in HSCs, hence elastic compatibility will be provided. This implies that higher strengths and higher strains at peak stresses will be obtained.

Based on the strain-gauge measurements in the model disc specimens with silica fume, higher tensile strain capacity values were recorded with respect to discs without silica fume. There is also a significant effect of silica fume replacement on the splitting tensile strength. The average splitting tensile strength values in disc specimens with and without silica fume were 4.56 and 3.52 N/mm^2, respectively. As shown in Fig. 12(a) in the disc without silica fume, the crack develops around the model aggregate resulting in a more tortuous and longer fracture path. In the disc with silica fume, a crack has not traversed the model aggregate, due to its shape and smooth surface and because of mismatch of matrix and aggregate, however the crack path was shorter and fracture was more brittle in nature. During the test, a central crack may start at the pole of the model aggregate towards the loading points, followed by wedge formation. As Hannant *et al.*[42] and Castro-Montero *et al.*[43] pointed out, the wedge formation constitues a secondary failure mode and occurs after a single crack has propagated through the diameter of the specimen.

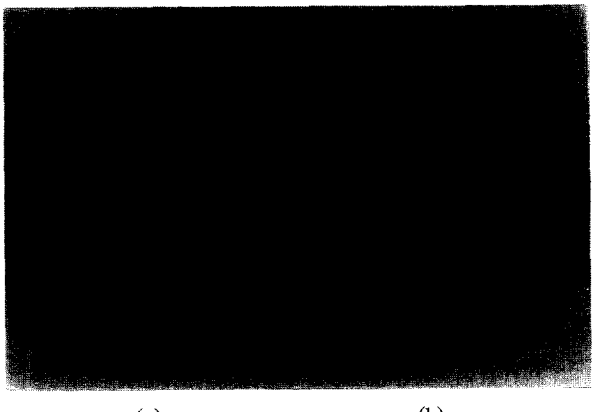

(a) (b)

Fig. 12. Failure modes of the model disc specimens: (a) without silica fume; (b) with silica fume.

Other model experiments for interface fracture

An example can be given for the typical interfacial fracture between non-silica fume mortar and model aggregate, as seen in Fig. 13. Crack initiation and propagation in rectangular blocks of mortar containing central cracks under compression were studied by Tasdemir *et al.*[44,45] using the fracture mechanics approach, finite element modelling and quantitative holographic interferometry. In their work, four different interfacial crack orientation angles, β (18°, 36°, 54° and 72°) were used, and specimens were made of mortar with a mix of 1:3:0.6 (cement:sand:water) by weight. Various stages of kink crack development are shown in Fig. 13 for a specimen with an aggregate–matrix interface notch inclined at an angle $\beta = 36°$. It is seen in Fig. 13(b) and (c) from such crack patterns that debonding at the aggregate–matrix interface always precedes the initiation of matrix cracking. In Maji's work[46], cracks were initiated at the model aggregate–matrix interfaces and after that were propagated parallel to the applied uniaxial compressive load. These types of experiments may be used in further studies for better understanding of HSCs with stronger interfaces.

In model experiments, however, it is difficult to get good workability and settlement during vibration. More vacant spaces may occur around model aggregate as compared to real concrete. From the microstructural point of view, a more realistic approach is required to investigate the interface in real concrete instead of mortar containing model aggregate. This is explained in the following section.

MICROSTRUCTURAL INVESTIGATIONS

As already noted, since the paste–aggregate transition zone is the weakest component, the mechanical behaviour of concrete is significantly

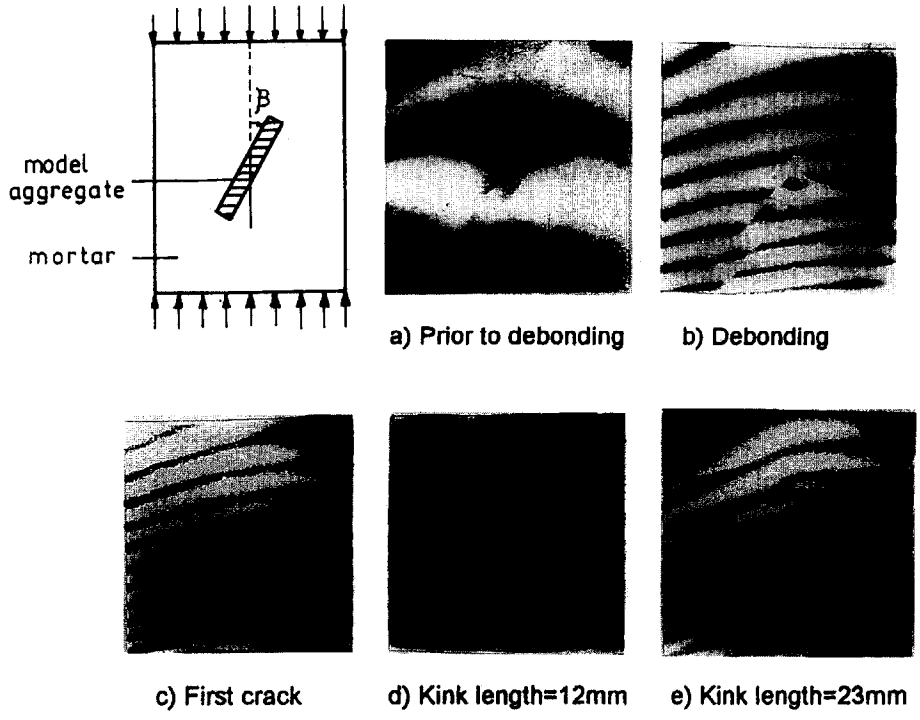

Fig. 13. Holographic fringes showing crack growth in a matrix for $\beta = 36°$.[45]

affected by the properties of that zone and the fracture of concrete is very sensitive to them.[10,11,47] Several research reports on microstructural investigation of the paste–aggregate transition zone have been published.[47–54]

After completion of bending,[10] uniaxial compression[36,47] and uniaxial tension[54] tests, the fracture surfaces were examined by Tasdemir *et al.*[10,47,54] using both a stereo microscope and a SEM/EDX (Scanning Electron Microscope/ Energy Dispersive X-Ray Analyzer) system. In concretes with silica fume, the cracks usually traversed through the aggregate; transgranular type fracture was observed and it was brittle in nature. In concretes without silica fume, however, the cracks usually developed around the coarse aggregate resulting in a more tortuous fracture path.

In concretes without silica fume, the SEM micrograph in Fig. 14(a) shows a profusion of

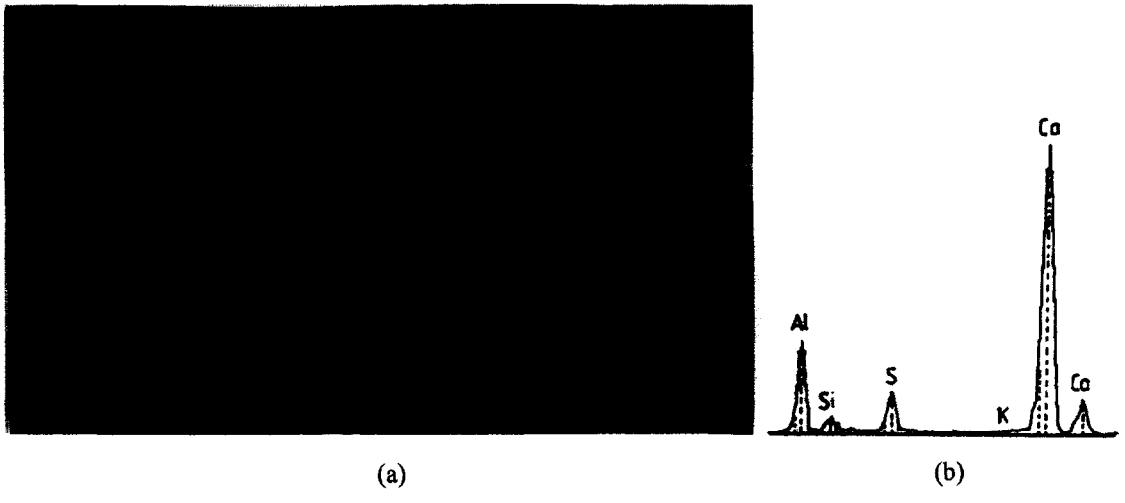

Fig. 14. (a) SEM micrograph at the paste–aggregate interface in concretes without silica fume; (b) the corresponding EDX spectrum confirms the AFm crystals.[47,55]

calcium hydroxide (CH) at the aggregate–paste interface. Not only are the CH crystals often very large in size, they are mostly tabular and oriented. This is a characteristic feature of normal concrete not containing any mineral admixture.[55] Apart from CH, some platy mono-sulphate (AFm) crystals were also identified in this region. The EDX spectrum confirms it as (AFm). The calcium silicate hydrate (C–S–H) is also much less dense. The paste was also porous and was characterized by the presence of fibrous or Type I C–S–H. Platy AFm and tabular CH crystals were also identifiable in the paste. The air voids were full of platy CH crystals.[47,55]

In concretes with silica fume, however, the interfacial zone is composed of dense C–S–H, as shown in Fig. 15(a). The air voids and other vacant spaces in this region are empty, and show no deposition of CH, mono-sulphate or ettringite (AFt) crystals. Dense paste identical to that of the interfacial zone is observed. As in the transition zone, the air voids in the paste are empty. Probe analysis of this region is indicated in the form of the EDX spectrum, shown in Fig. 15(b).[55]

The observation of abundant CH crystals at the paste–aggregate interface in the non-silica fume concrete corresponds well with those of others.[1,11] It is well known that the interplanar compressive strength of CH crystals is extremly low, in the range of 1–2 N/mm^2. Therefore, it is not surprising to note that under uniaxial compression, tension, bending and torsion, failure occurs in this zone, which is defined as the inter-aggregate type of fracture. In contrast, the interfacial zone in HSCs is characterized by a direct link between the aggregate and cement paste C–S–H at this interface; this is in lieu of CH crystals.[47,55] As a result of this strong bonding, the matrix composed of paste and aggregates acts as a composite material. Under these loading conditions, integral fracture of the entire composite occurs, rather than failure of individual weak components. The difference in the paste–aggregate interfacial microstructure of silica fume and non-silica fume concrete is attributable to the pozzolanic reaction of silica fume which consumes the CH normally concentrated in this zone; it is replaced by dense C–S–H. Based on recent advances, however, it can also be concluded that the filler effect of silica fume may be as important as its pozzolanic effect.[50,56,57] Thus, HSCs containing both silica fume and superplasticizer become stronger, less heterogeneous, more dense, with less stress-induced microcracking under loads and higher strain values at peak stresses; then the fracture occurs in a more brittle manner.

TRANSITION BETWEEN NSCS AND LLCS

NSCs and low strength lightweight concretes (LLCs) are heterogeneous materials, however semi-lightweight concretes (SLCs) are extremely heterogeneous, because SLCs contain both lightweight and normal weight aggregates. A

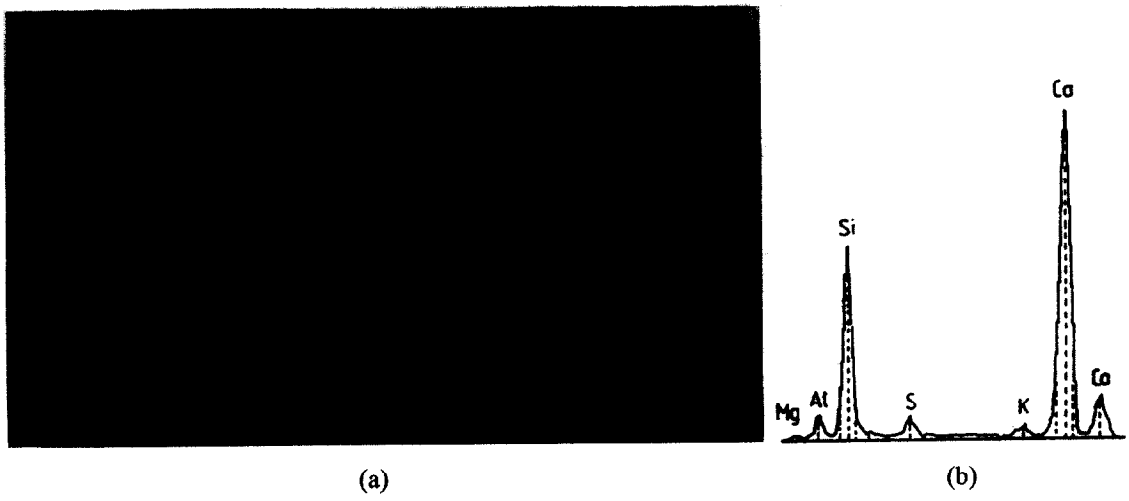

Fig. 15. (a) SEM micrograph at the paste–aggregate interface in concretes with silica fume; (b) the Si peak confirms dense C–S–H at the interface. Apart from Ca and Si, a small but detectable amount of Al, S and K are present in the C–S–H.[47,55]

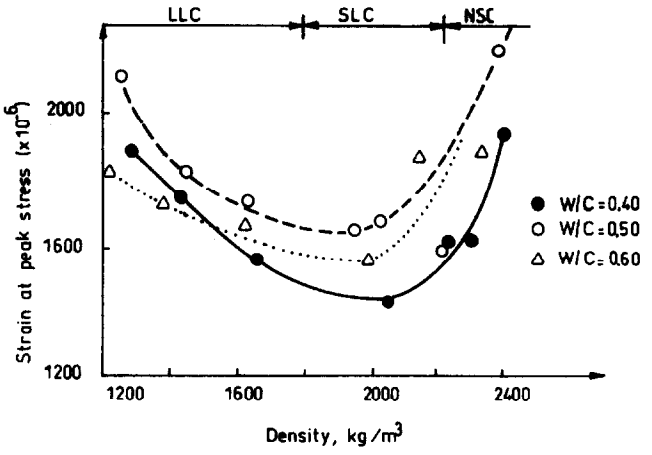

Fig. 16. Strain at compressive strength versus density of concrete.[21]

typical indication of elastic mismatching of constituents in concrete is the case of SLCs. In Tasdemir's work,[21] the maximum particle size, grading and cement content of a normal aggregate concrete were kept constant, and for each aggregate fraction the same volume of normal aggregate was replaced by softer natural lightweight aggregate particles: pumice. As shown in Fig. 16, in concretes with three different effective water/cement ratios, the strains at peak stresses in compression show a minimum in the zone of SLCs. In both NSCs and LLCs, higher values of strains were obtained due to the elastic matching of the constituents.

CONCLUSIONS

Based on the evaluation of published test results on the three-phase composite material model proposed, on model test results and on examinations of fracture surfaces and microstructural studies at the aggregate–matrix interfaces, the following conclusions can be drawn:

1. The results obtained show that the higher the compressive strength the higher the strains at peak stresses in compression, bending, tension and torsion for a wide range of concrete strengths.
2. In NSCs, large tangential, radial and shear stresses occur at the interface due to the elastic mismatch of the aggregate and the matrix. In both HSCs and LCs, however, the elastic modulus of the aggregate is closer to that of the matrix and lower tangential stress distributions occur at the aggregate–matrix interface.
3. In both HSCs and LCs, cracks will be forced to pass through the aggregate due to tensile stresses occurring at the pole (at the tip of the aggregate) and also high levels of tangential stresses occur in the matrix close to the interface or at the aggregate surface.
4. The relative absorbed energy up to peak stress in compression decreases significantly with an increase in compressive strength of the concrete, which also indicates increased brittleness.
5. Based on fracture surface examinations using both a stereo microscope and a scanning electron microscope (SEM) after completion of some additional compression, bending and tension tests, it is observed that in concrete without silica fume the cement–aggregate interface had a profusion of calcium hydroxide and also much less dense calcium silicate hydrate than the bulk C–S–H, and hence the cracks usually develop at the weak interface, i.e. around the coarse aggregate, resulting in an inter-coarse aggregate type of fracture. However, in the case of the strong interface (in concretes with silica fume), the interfacial zone becomes stronger, more homogeneous and dense, less stress induced microcracking occurs at the interface, and hence the cracks usually pass through the aggregates; transgranular type of fracture is observed, and the fracture surfaces are less tortuous due to the nature of typical brittle behaviour.
6. Both the three-phase composite model proposed and additional microstructural studies done at the aggregate–cement paste interface, show that for compression, tension, torsion and bending cases, when HSCs and LCs are subjected to external loads, more linear ascending branches and higher values of strains at peak stresses are obtained due to the elastic matching of the constituents and the reduced microcracking.
7. For three different water/cement ratios, the strains at peak stresses in compression show a significant minimum in the zone of semi-lightweight concretes due to their hetereogeneous structures.

ACKNOWLEDGEMENTS

This research was completed at the University of Wales Cardiff (UWC). The first author

wishes to acknowledge the financial support of UWC during his visit. For the material modelling part of this work, the support of TÜBITAK (The Scientific and Technical Research Council of Turkey)–INTAG (Construction Technologies Research Grant Committee) (Grant:INTAG-616), is also acknowledged.

REFERENCES

1. Skalny, J. P. (ed.), *Materials Science of Concrete I*. The American Ceramic Society, Westerville, OH, 1989.
2. Tasdemir, M. A., Lydon, F. D. & Barr, B. I. G., The tensile strain capacity of concrete. *Magazine of Concrete Research*, **48** (1996) 211–218.
3. De Nicola, B., Pani, L. & Pozzo, E., Strain of concrete at peak compressive stress for a wide range of strengths. *Materials and Structures*, **27** (1994) 206–210.
4. Welch, G. B., Tensile strains in unreinforced concrete beams. *Magazine of Concrete Research*, **18** (1966) 9–18.
5. Oladapo, I. O., Cracking and failure in plain concrete beams. *Magazine of Concrete Research*, **16** (1964) 103–110.
6. Giovambattista, A., Violini, D. & Zerbino, R., Extensibility of high-strength concretes. *Materials and Structures*, **25** (1992) 552–557.
7. Brooks, J. J., Bennett, E. W. & Owens, P. L., Influence of lightweight aggregates on thermal strain capacity of concrete. *Magazine of Concrete Research*, **39** (1987) 60–72.
8. Wittmann, F. H., Structure of concrete with respect to crack formation. In *Fracture Mechanics of Concrete*, ed. F. H. Wittmann. Elsevier Applied Science, Amsterdam, 1983, pp. 43–74.
9. Bentur, A., Microstructure of high strength concrete. *Darmstädter Massivbau-Seminar, THD, Darmstadt*, **6** (1991) 1–16.
10. Tasdemir, C., Tasdemir, M. A., Lydon, F. D. & Barr, B. I. G., Effects of silica fume and aggregate size on the brittleness of concrete. *Cement and Concrete Research*, **26** (1996) 63–68.
11. Sarkar, S. L., The importance of microstructure in evaluating concrete. In *Advances in Concrete Technology*, ed. V. M. Malhotra, Second Edition. CANMET, Ottawa, 1994, pp. 125–160.
12. Swamy, N., Aggregate–matrix interaction in concrete systems. In *Proceedings of Civil Engineering Materials Conference (1969), Part I*, Southampton. John Wiley Interscience, London, 1971, pp. 301–315.
13. Hsu, T. T. C., Slate, F. O., Sturman, G. M. & Winter, G., Microcracking of plain concrete and the shape of the stress–strain curve. *ACI Journal*, **60** (1963) 209–224.
14. Hsu, T. T. C., Mathematical analysis of shrinkage stress in a model of hardened concrete. *ACI Journal*, **60** (1963) 371–390.
15. Shah, S. P. & Chandra, S., Critical stress, volume change, and microcracking of concrete. *ACI Journal*, **65** (1968) 770–781.
16. Nilson, A. H., High-strength concrete: An overview of Cornell research. In *Utilization of HSC, Proceedings of Symposium in Stavanger, Trondheim*. 1987, pp. 27–37.
17. Smeplass, S., *High Strength Concrete: Mechanical Properties — Normal Density Concretes*. SP4-Materials Design, Report 4.4, SINTEF, Trondheim, 1992.
18. Jansen, D. C., Shah, S. P. & Rossow, E., Stress–strain results of concrete from circumferential strain feedback control testing. *ACI Materials Journal*, **92** (1995) 419–428.
19. Moral, H., Effects of the structure of binding cement paste on the inelastic behaviour of concrete and mortars under short-term compressive loading. M.S. Thesis, Faculty of Civil Engineering, Istanbul Technical University, 1979 (in Turkish with English Summary).
20. Oktar, O. N., Role of structure of binding cement paste on the inelastic behaviour of concrete under short-term compressive loading. Ph.D. Thesis, Faculty of Civil Engineering, Istanbul Technical University, 1977 (in Turkish with French Summary).
21. Tasdemir, M. A., Elastic and inelastic behaviour of structural lightweight aggregate concretes. Ph.D. Thesis, Faculty of Civil Engineering, Istanbul Technical University, 1982 (in Turkish with English Summary).
22. Kaar, P. H., Hanson, N. W. & Capell, H. T., Stress–strain characteristics of high strength concretes. Research and Development Bulletin, RD051-0ID, PCA, Skokie, IL, 1977.
23. Yildirim, H., Effects of composition on the mechanical behaviour of semi-lightweight concretes under cyclic loading conditions. M.S. Thesis, Faculty of Civil Engineering, Istanbul Technical University, 1989 (in Turkish with English Summary).
24. Bischoff, P. H. & Perry, S. H., Impact behaviour of plain concrete loaded in uniaxial compression. *Journal of Engineering Mechanics, ASCE*, **121** (1995) 685–693.
25. Carrasquillo, R. L., Nilson, A. H. & Slate, F. O., Properties of high strength concrete subject to short-term loads. *ACI Journal*, **78** (1981) 171–177.
26. Dilger, W. H., Koch, R. & Kowalczyk, R., Ductility of plain and confined concrete under different strain rates. *ACI Journal*, **81** (1984) 73–81.
27. Ahmad, S. H. & Shah, S. P., Behaviour of hoop confined concrete under high strain rates. *ACI Journal*, **82** (1985) 634–647.
28. Ahmad, S. H. & Shah, S. P., Stress–strain curves of concrete confined by spiral reinforcement. *ACI Journal*, **79** (1982) 484–490.
29. Smeplass, S., *High Strength Concrete: Mechanical Properties — lwa Concretes*. SP4 Materials Design, Report 4.5., SINTEF, Trondheim, 1992.
30. Balendran, R. V., Properties of high strength lightweight concrete. Ph.D. Thesis, University of Wales, Cardiff, 1980.
31. Phillips, D. V. & Zhang, B., Direct tension tests on notched and unnotched plain concrete specimens. *Magazine of Concrete Research*, **45** (1993) 25–35.
32. Guo, Z. & Zhang, X., Investigation of complete stress–deformation curves for concrete in tension. *ACI Materials Journal*, **84** (1987) 278–285.
33. Xie, N. & Liu, W., Determining tensile properties of mass concrete by direct tensile test. *ACI Materials Journal*, **86** (1989) 214–219.
34. Brokenshire, D. R., A study of torsion fracture tests. Ph.D. Thesis, University of Wales Cardiff, 1995.
35. Bremner, T. W., Influence of aggregate structure on low density concrete. Ph.D. Thesis, University of London, Imperial College of Science and Technology, 1981.
36. Tasdemir, C., Effect of aggregate–cement paste interface on the fracture parameters of high strength concretes. Ph.D. Thesis, Istanbul Technical University, 1995 (in Turkish with English Summary).
37. Akyüz, S., A solution of the problem of double inclusions with cartesian axes symmetry in an infinite plate.

Ph.D. Thesis, Faculty of Civil Engrg., Istanbul Technical University, 1971 (in Turkish with French Summary).
38. Akyüz, S., A solution of the problem of circular inclusions with the regular hexagonal symmetry in an infinite plate. In *6th National Mechanics Congress*, Vol.1. 1990, pp. 86–101 (in Turkish with English Abstract).
39. Inan, M., *Theory of Elasticity in Plane*. Matbaa Teknisyenleri Basimevi, Istanbul, 1963 (in Turkish).
40. Little, R. Wm., *Elasticity*. Civil Engrg. and Engrg. Mech. Series, eds. N.M.Newmark and W.J.Hall, Prentice-Hall Inc., New Jersey, 1973.
41. Bremner, T. W. & Holm, T. A., Elastic compatibility and the behaviour of concrete. *ACI Journal*, **83** (1986) 244–250.
42. Hannant, D. J., Buckley, K. J. & Croft, J., The effect of aggregate size on the use of the cylinder splitting test as a measure of tensile strength. *Materials and Structures, RILEM*, **6** (1973) 15–21.
43. Castro-Montero, A., Jia, Z. & Shah, S. P., Evaluation of damage in Brazilian test using holographic interferometry. *ACI Materials Journal*, **92** (1995) 268–275.
44. Tasdemir, M. A., Maji, A. K. & Shah, S. P., Crack growth in concrete under combined mode I and mode II. *Bulletin of Istanbul Technical University*, **45** (1992) 133–164.
45. Tasdemir, M. A., Maji, A. K. & Shah, S. P., Crack propagation in concrete under compression. *Journal of Engineering Mechanics, ASCE*, **116** (1987) 137–150.
46. Maji, A. K., Study of concrete fracture using acoustic emission and laser holography. Ph.D. Thesis, Northwestern University, Evanston, IL, 1989.
47. Tasdemir, C., Sarkar, S. L., Tasdemir, M. A., Akyüz, S. & Koca, C., Effect of silica fume on the brittlenes of high strength concretes under compression. In *Proc. XIth European Ready Mixed Concrete Congress*, Istanbul, 1995, pp. 444–452.
48. Mindess, S. & Shah, S. P. (Eds.), *Bonding in Cementitious Composites*. Proc. Sym., MRS, Pittsburgh, 1988.
49. Maso, M. (Ed.), *Interfaces in Cementitious Composites, Proc. RILEM Int.Conf.*, eds E. Toulouse and F. N. Spon. London, 1992.
50. Goldman, A. & Bentur, A., Bond effect in high-strength silica-fume concretes. *ACI Materials Journal*, **86** (1989) 440
51. Monteiro, P. J. M. & Mehta, P. K., Ettringite formation on the aggregate cement paste interface. *Cement and Concrete Research*, **15** (1985) 378–380.
52. Larbi, I. A., Misrostructure of the interfacial zone around aggregate particles in concrete. *Heron, Delft* **38**(1) (1993).
53. Mindess, S., Interfaces in concrete. In *Materials Science of Concrete I*, ed. J. P. Skalny. American Ceramics Society, 1989, pp. 163–180.
54. Tasdemir, C., Tasdemir, M. A., Grimm, R. & König, G., Microstructural effects on the brittleness of high strength concretes. In *FAMCOS-2:2nd Int.Conf. Frac. Mech. Concr. and Concr. Struct.* ed. F. H. Wittmann, Vol. 1. Aedificatio Publishers, 1995, pp. 125–134.
55. Sarkar, S. L. Private communications, 1993, 1995.
56. Goldman, A. & Bentur, A., Properties of cementitious systems containing silica fume or non-reactive microfillers. *Advances in Cement Based Materials*, **1** (1994) 209–215.
57. Detwiller, R. J. & Mehta, P. K., Chemical and physical effects of silica fume on the mechanical behaviour of concrete. *ACI Materials Journal*, **86** (1989) 609–614.